We are IntechOpen, the world's leading publisher of Open Access books
Built by scientists, for scientists

6,900
Open access books available

185,000
International authors and editors

200M
Downloads

Our authors are among the

154
Countries delivered to

TOP 1%
most cited scientists

12.2%
Contributors from top 500 universities

WEB OF SCIENCE™

Selection of our books indexed in the Book Citation Index in Web of Science™ Core Collection (BKCI)

Interested in publishing with us?
Contact book.department@intechopen.com

Numbers displayed above are based on latest data collected.
For more information visit www.intechopen.com

2

Heterostructured III-V Nanowires with Mixed Crystal Phases Grown by Au-assisted Molecular Beam Epitaxy

D.L. Dheeraj, H.L. Zhou, A.F. Moses, T.B. Hoang, A.T.J. van Helvoort, B.O. Fimland and H. Weman
Norwegian University of Science and Technology
Norway

1. Introduction

Nanowires (NWs) with diameters in the range of few 10s of nanometers and lengths up to few micrometers long are one-dimensional materials that have attracted a great deal of interest recently in various fields, including photonics, electronics and medicine. These one-dimensional materials can offer improvement in the performance of optical and electronic devices due to their size-induced quantum confinement effects. In addition, their high surface area to volume ratio makes them potential candidates for various sensor applications. Several review articles reporting about the properties and applications of NWs made of different materials have already been published (Tian et al., 2009; Agarwal, 2008; Schmidt et al., 2009; Agarwal & Lieber, 2006; Lauhon et al., 2004). In this book chapter, we focus on heterostructured III-V semiconductor NWs with increased potential for use in photonic applications grown by molecular beam epitaxy.

Most optoelectronic devices are fabricated by using various III-V materials, because of their direct bandgap nature. The efficiency of these devices have improved substantially in the last 5 decades by reducing the dimensions of these materials, reducing defect density and changing the design using e.g. quantum wells (QW), multiple QWs, superlattice heterostructures and quantum dots (QDs) in the active layers. QWs consist of a very thin layer of a material with a lower bandgap sandwiched between materials with a higher bandgap. Such structures not only confine the carriers in the growth direction but also passivate surface states at the lower bandgap material surface. However, the choice of materials for the growth of defect free heterostructures is limited by the lattice mismatch of different materials. This is also one of the main reasons inhibiting the integration of III-V materials on Si. Such problems can be avoided in the growth of NWs, which provides the provision to relax in the radial direction without forming any dislocations. In fact, several successful NW based heterostructures, including structures with lattice mismatch as large as 7.8%, has been reported (Guo et al., 2006).

1.1 Vapor-Liquid-Solid growth mechanism

Fabrication of NWs by the bottom-up approach was first demonstrated by Wagner and Ellis in 1964, and the technique was named as vapor-liquid-solid (VLS) growth. This technique

Source: Nanowires, Book edited by: Paola Prete,
ISBN 978-953-7619-79-4, pp. 414, March 2010, INTECH, Croatia, downloaded from SCIYO.COM

uses a metal particle (often Au) as a catalyst, which forms a liquid-alloy particle on reacting with source materials supplied in vapor form. On supplying the source material continuously to this liquid-alloy, the excess material dissolved in it precipitates in the form of a solid NW at the bottom of the particle (Wu & Yang et al., 2001). The diameter and position of the NW are defined by the Au particle. As shown in Fig. 1, the Ga adatoms hitting the substrate surface diffuse to the Au droplet along the NW sidewall. With this technique, it is possible to tailor the composition of the NW in both the axial and radial directions. The different steps involved in the VLS growth mechanism are shown in Fig. 1.

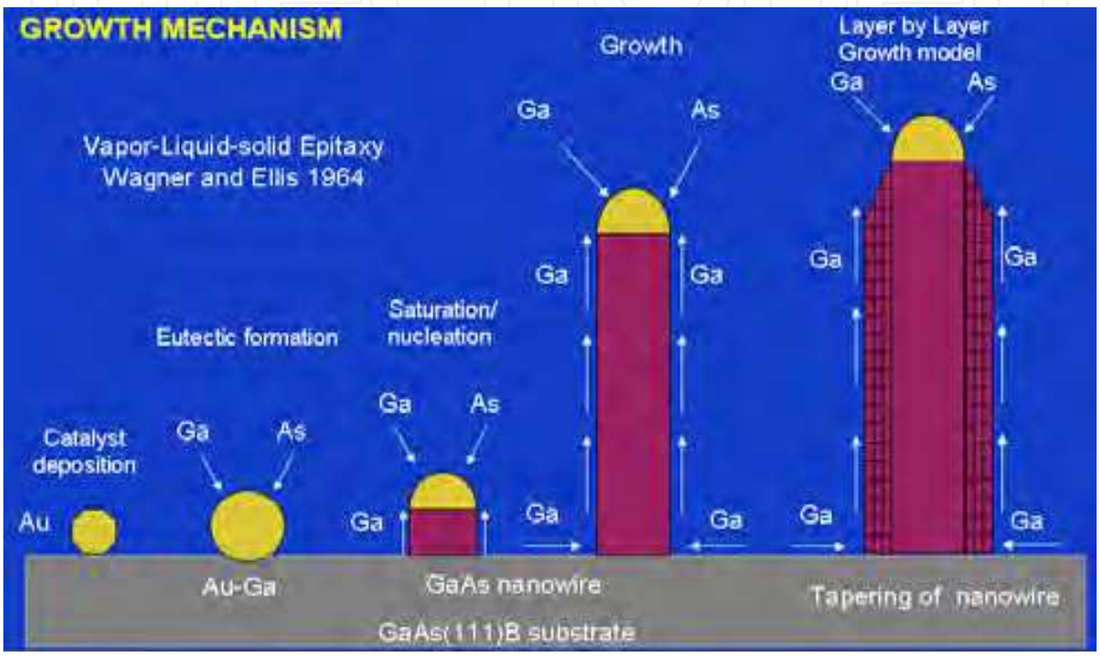

Fig. 1. Schematic diagram showing the various steps in the VLS growth of a GaAs NW.

As the NWs grow longer, tapering of the NWs is often observed. There are mainly two arguments explaining the reason for tapering: the first reason is based on the decrease in diameter of the Au droplet and hence the NW with its length due to the decrease of incoming Ga flux to the Au droplet (Harmand et al., 2005), while the second reason is explained by the (radial) layer-by-layer growth mechanism which would become effective when the length of the NW exceeds the diffusion length of Ga adatoms on the NW sidewall (Chen et al., 2006).

NWs have been grown by using the VLS growth technique in most III–V materials combinations, on native substrates as well as on silicon (Ihn et al., 2007; Tomioka et al., 2009), and with several epitaxial techniques, including metal organic vapor phase epitaxy (MOVPE), chemical beam epitaxy (CBE) and molecular beam epitaxy (MBE). Over the past decade, there has been considerable interest focused on the growth of heterostructured NWs (both axial and radial core-shell structures), followed by the first demonstrations of device prototypes, such as light-emitting diodes (Minot et al., 2007; Svensson et al., 2008;), high electron mobility devices (Jiang et al., 2007), laser-diodes (Duan et al., 2003), and photovoltaic cells (Czban et al., 2009).

1.2 Molecular beam epitaxial growth of NWs

MBE is one of the most controllable and widely used non-equilibrium growth techniques for growing thin, epitaxial films of a wide variety of materials. The deposition of material on the substrate is performed by evaporating the material from the effusion cells in a chamber maintained under ultrahigh vacuum. The deposition performed in an ultrahigh vacuum chamber not only makes it possible to grow highly pure materials but also to install in-situ characterization techniques such as reflection high-energy electron diffraction (RHEED). A deposition rate as low as 0.1 ML/s can be achieved by changing the temperature of the effusion cell. In addition, a flux of molecules or atoms towards the substrate can be abruptly released (or blocked) by controlling the shutters in front of the cell. This allows growing heterostructures with abrupt interfaces. Another major difference between the MBE growth method and other growth techniques is that it is far from thermodynamic equilibrium conditions, i.e., it is mainly governed by the kinetics of the surface processes.

The growth of NWs by the VLS mechanism in MBE was initially speculated to be impossible due to that the material is supplied in the form of atoms, where no catalytic activity of Au to decompose the metallic groups to atoms is required as in metal-organic chemical vapor deposition. However, these speculations were proven to be incomplete since several groups have demonstrated the growth of GaAs NWs by MBE (Wu et al., 2002; Cirlin et al., 2005; Harmand et al., 2005; Plante and LaPierre, 2006). Furthermore, remarkable progress has also been shown in self-catalyst growth of GaAs NWs by MBE (Fontcuberta i Morral et al., 2008).

The Au-assisted process of NW growth in MBE is explained to be a thermodynamic process due to which the group III adatoms diffuse from the substrate surface, which is at a higher chemical potential as compared to the Au droplet, which has lower chemical potential (Harmand et al., 2006). On the other hand, it has also been shown that the kinetic processes involved in the NW growth also play an important role during the NW growth, and are a bit different than those during the thin-film growth. The major kinetic processes involved during the growth of NWs by Au-assisted MBE are schematically shown in Fig. 2.

The dependence of the (axial) growth rate of NWs in the MBE process on the NW diameter is found to be different from that of the observations made on the NW growth by the CVD process (Givargizov, 1975). It is observed that the MBE growth rate of the NWs decreases with increase in the diameter of NWs (Plante & LaPierre, 2006). This was theoretically explained by Dubrovskii et al., 2005, attributing the diameter dependence of the NW growth to the diffusion of group III adatoms from the substrate surface to the Au particle.

The demonstrations of the growth of homogeneous binary compound NWs, including GaAs, InP, InAs and GaP by MBE (Cornet et al., 2007; Harmand et al., 2005; Ihn & Song, 2007) were followed by the growth of heterostructures involving ternary compounds such as AlGaAs, InGaAs, GaAsSb, InAsP and GaAsP (Chen et al., 2006; Chen et al., 2007; Cornet & LaPierre, 2007, Dheeraj et al., 2008a, Tchernycheva et al., 2007). However, the progress in the MBE growth of ternary compound NWs involving different group III elements, such as AlGaAs and InGaAs, has been inhibited due to difficulties in obtaining uniform composition along the length of the NW. This problem arises due to the difference in diffusion lengths of different group III elements along the NW sidewall. On the other hand, no variation in composition along the NW has been reported for the ternary compound NWs involving different group V elements such as InAsP and GaAsP. This could be due to the longer diffusion lengths of group V elements compared to that of the group III elements. The variation in composition could, however, be quite small in short NWs or inserts involving ternary structures.

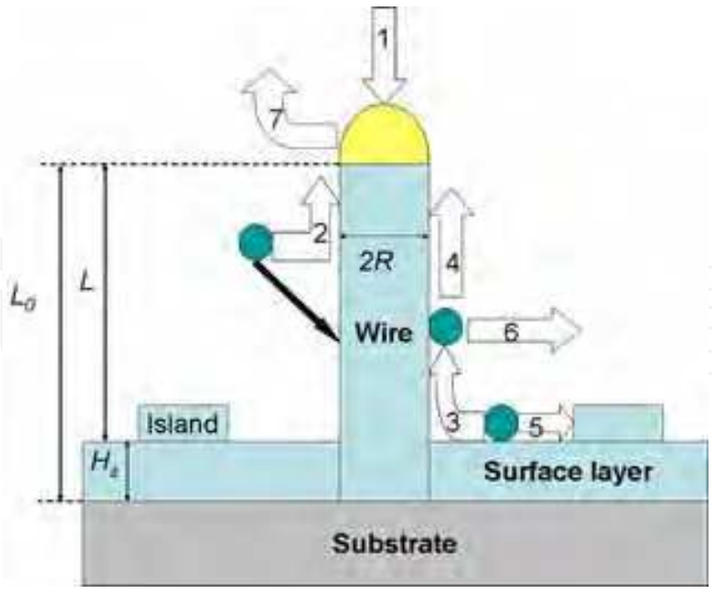

Fig. 2. The model of Au-assisted NW growth by MBE: The different pathways for adatoms are through; 1) direct impingement, 2) diffusion flux from the side walls to the droplet, 3) diffusion from the substrate to the sidewalls, 4) diffusion from the substrate along the sidewalls to the droplet, 5) nucleation on the surface, 6) desorption from the sidewalls, 7) desorption from the droplet (Dubrovskii & Sibirev, 2007).

Despite the fast progress in the growth of heterostructured NWs by MBE, the understanding and control of the crystal structure of these NWs is a challenging task. In fact, most of the III-V NWs grown by MBE adapt wurtzite (WZ) crystalline structure, even though the III-V materials exhibit zinc-blende (ZB) structure in bulk form. Since the WZ crystalline structure is not a stable form of these materials, the NWs often exhibit a high density of crystal defects (stacking faults, twins) irregularly within the NWs. A stacking fault in a WZ phase inherently forms a unit cell of ZB segment, while a twin in a ZB phase inherently forms a unit cell of a WZ segment (Caroff et al., 2009). It is very important to reduce the density of such crystal defects since they deteriorate the optical and electrical properties of the NWs.
Due to that the NWs have been found to form with different crystal phases depending on the growth conditions, this now allows for *heterocrystalline* band-structure engineering. This includes crystal phase-modulated as well as combined crystal phase- and crystal material-modulated heterostructures. This is because III-V materials in the ZB form have different band gap and different band offsets compared to that in the WZ form. Therefore, heterojunctions form in the same material wherever the material changes its crystalline phase. Recently, some research groups have shown the ability to control the crystal structure in MOCVD grown NWs (Caroff et al., 2009; Algra et al., 2008). Despite of a few successful attempts in controlling stacking faults in NWs grown by MBE, it is still a challenging task to understand the factors influencing the crystal structure (Shtrikman et al., 2009; Patriarche 2008).
Although the WZ crystal phase of GaAs in NWs has been achieved by many groups by now, little is known about its electronic and optical properties. Several works have attempted to determine the band gap in WZ GaAs NWs but the results are still inconsistent (Zanolli et al., 2007; Martelli et al., 2007; Moewe et al., 2008). As mentioned earlier, stacking faults in the

WZ phase inherently possess the ZB phase. Depending on the conduction and valence band offset energies in the ZB crystal structure with respect to WZ, even a low density of ZB segments could trap most of the photo-excited electrons and/or holes. As a result, one may observe that the dominating photoluminescence related emission in such NWs occur at energies close to (type I band offsets) or even below (type II band offsets) the band gap energy of ZB GaAs even if the band gap is higher for WZ GaAs.

1.3 Overview of the book chapter

In this book chapter, we will discuss the structural and optical properties of axial and radial heterostructured III-V NWs with mixed crystal phases grown by Au-assisted MBE.

Our GaAs NWs are observed to exhibit WZ crystalline structure and often stacking faults (SFs) are randomly distributed in the NW. Interestingly, by incorporating Sb in the GaAs NWs, we have found that GaAsSb NWs form in the ZB crystalline structure with very few twin defects (Dheeraj et al., 2008a). Recently, we have demonstrated the growth and characterized the optical properties of single and multiple SF-free ZB GaAsSb inserts in WZ GaAs NWs (Dheeraj et al., 2008b; Dheeraj et al., 2009). The growth of GaAs NWs with multiple GaAsSb inserts enabled us to conclude that the growth rate of NWs changes with growth time due to the inclined molecular beam in the growth chamber, and revealed the growth parameters influencing the formation of SFs as we will demonstrate within this chapter.

Micro-photoluminescence (μ-PL) characterization of SF-free WZ GaAs NWs reveals that the bandgap of WZ GaAs is ~ 29 meV larger than that of ZB GaAs (Hoang et al., 2009). Further, we demonstrate the growth procedure of GaAs/AlGaAs radial heterostructured core-shell NWs, with strongly enhanced photoluminescence efficiency from the GaAs core due to the shell passivation of surface states (Zhou et al., 2009). The structural characterization of these NWs by high resolution transmission electron microscopy (HRTEM) shows that the shell copies the crystalline structure of the core NW.

Finally, we discuss the growth of single GaAs/AlGaAs core-shell NWs with axial GaAsSb core-inserts. We demonstrate that it is possible to change the crystal phase of GaAs at the upper GaAsSb/GaAs interface by introducing a growth interruption. By changing the GaAs crystal phase above the insert from ZB to WZ, we observe dramatic changes in the photoluminescence properties, explained to be due to that the heterojunction band alignment is changed from type II to type I.

2. Experimental procedure

The NWs were grown in either a Varian Gen II Modular or a Riber 32 MBE system equipped with a Ga dual filament cell, an Sb cracker cell, and an As valved cracker cell, allowing to fix the proportion of dimers and tetramers. In the present study, the major species of arsenic and antimony were As_4 and Sb_2, respectively. The substrate surface was first deoxidized at 620°C, and then a 60 nm thick GaAs buffer, a 72 nm thick $Al_{0.33}Ga_{0.67}As$ film and a 36 nm thick GaAs film were grown under growth conditions producing an atomically flat surface (Yang et al., 1992). The AlGaAs film embedded in the GaAs buffer can be used as a marker to distinguish between the GaAs buffer and the 2D GaAs grown during the growth of the NWs. The GaAs/AlGaAs/GaAs heterostructure was capped with an amorphous As layer to avoid oxidation during its transfer in ambient air to an electron-beam evaporation system

for gold deposition. The As cap was then desorbed at 280°C under high vacuum (10^{-7} Torr) in the electron-beam evaporation chamber (Bernstein et al., 1992). A ~ 1 nm thick Au film, as determined by a quartz crystal thickness monitor, was deposited on the sample surface. The sample was then transferred to and loaded into the MBE system. Under an As_4 flux of 6×10^{-6} Torr, the substrate temperature was increased to 540°C, a temperature suitable for GaAs NW growth. At this stage, nanoparticles containing Au alloyed with the substrate constituents were formed. GaAs NW growth was initiated by opening the shutter of the Ga effusion cell. The temperature of the Ga effusion cell was preset to yield a nominal planar growth rate of 0.7 ML/s. The Sb shutter was also opened to supply an Sb_2 flux of 6×10^{-7} Torr to grow GaAsSb NWs, whenever needed.

Morphological characterization of NWs was performed in a Zeiss Supra field-emission scanning electron microscopy (FE-SEM) operating at 5 kV. Crystalline structure was analyzed in either a Philips CM20, Philips CM30 or Jeol 2010F TEM operating at 200 kV and equipped with an Oxford instruments INCA energy dispersive X-ray (EDX) spectrometer for composition measurements. For TEM characterization, the NWs were scrapped off from the substrate and transferred to a Cu grid with a lacey carbon film. A more detailed report on the TEM techniques used for characterization of NWs can be found in Van Helvoort et al., 2009.

The crystallographic orientation of the NW ensembles on as-grown substrates was checked by X-ray diffraction (XRD) pole figure measurements (Largeau et al., 2008) carried out with a PANalytical X'Pert Pro MRD diffractometer with a point focus configuration defined by a poly capillary lens and crossed slits.

μ-PL measurements were carried out using an Attocube CFMI optical cryostat. Samples were placed in a He exchange gas and kept at a temperature of 4.4 K. For temperature dependent measurements, the sample can be heated up to 70 K. Single NWs were excited by a 633 nm laser line. The laser was defocused onto the NWs with an excitation density of approximately 1 $kWcm^{-2}$ using a 0.65 numerical aperture objective lens. The μ-PL from single NWs was dispersed by a 0.55 m focal length Jobin-Yvon spectrograph and detected by an Andor Newton thermo-electrically cooled Si CCD camera. The spectral resolution of the system is ~ 200 μeV. For single NW measurements, NWs were removed from their grown substrate and dispersed on a Si substrate with an average density of ~ 0.1 NW per μm^2.

3. Results

3.1 Growth of GaAsSb NWs

GaAs NWs were grown for 5 minutes and GaAsSb NWs for 20 minutes on GaAs(111)B substrates. Typical 45° tilted (Fig. 3(a)) and top-view (Fig. 3(b)) SEM images show the GaAsSb NWs with their Au catalyst and a growth axis normal to the GaAs(111)B surface. Diameters of the NWs range from 30 to 100 nm and are nearly uniform along the NW, except at the base which is broader than the rest of the NW. The top-view image (Fig. 3(b)) shows a hexagonal cross sectional shape of the NW as well as at the base region. The length and diameter of the NWs was measured from the SEM images. The NW length is observed to decrease with increase in NW diameter (Dheeraj et al., 2008a). This dependence of NW length on diameter confirms that growth is to a large extent fed by diffusion of adatoms from the surface of the substrate to the Au droplet at top of the NWs, as described by Dubrovskii & Sibirev, 2007.

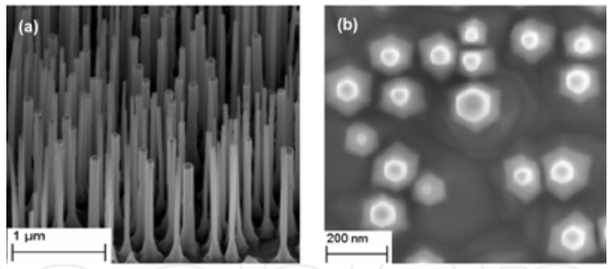

Fig. 3. (a) 45° tilted view and (b) top view SEM images of as-grown GaAsSb NWs grown on a GaAs(111)B substrate by Au-assisted MBE (Dheeraj et al., 2008a).

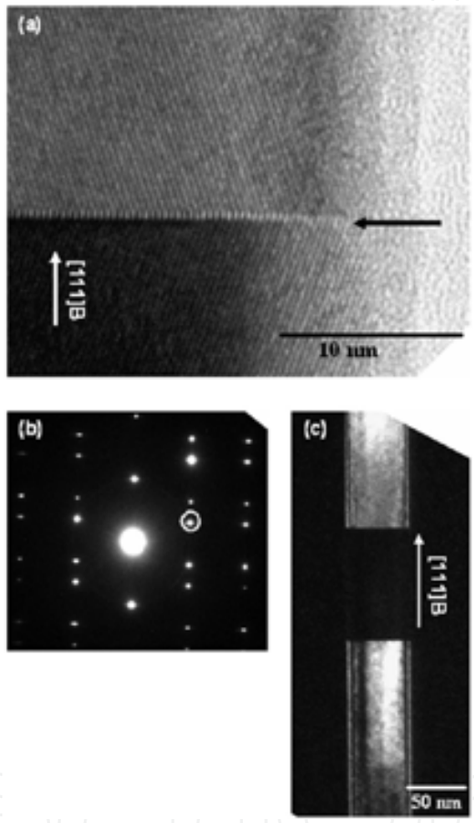

Fig. 4. (a) High resolution TEM image and (b) electron diffraction pattern showing the ZB structure with twins. (c) Dark-field image obtained by using the $1\,\bar{1}\,1$ diffraction spot, marked by a circle in Fig. 4(b) (Dheeraj et al., 2008a).

In Fig. 4, we show TEM images of a typical GaAsSb NW. The most striking feature of our experimental results is that our GaAsSb NWs adapt ZB structure, whereas the same growth conditions (except the Sb flux) produce GaAs NWs with WZ structure, as commonly observed for [111]B-oriented NWs grown by MBE. Fig. 4(a) shows a [110] zone axis HRTEM image revealing the ZB structure of the GaAsSb NW, with a twinning plane (indicated by black arrow) perpendicular to the [111]B growth axis. The crystal planes above the twinning plane (orientation A) is a rotation by 60° relative to the crystal planes below the twinning plane (orientation B) about the growth axis. The selected area electron diffraction (SAED)

pattern in Fig. 4(b) shows additional spots related to the presence of both crystal orientations. Using the $1\,\bar{1}\,1$ diffraction spot marked by a circle in Fig. 4(b), we obtained the dark field image as shown in Fig. 4(c), where crystal orientation A appears bright and the crystal orientation B dark. By investigating the full length of several NWs, single-oriented ZB segments as long as 500 nm were observed. We have also demonstrated a technique to determine the average volumes of crystal orientation A and B parts of GaAsSb NW ensembles by XRD pole figure measurements, and found the volumes to be of equal ratio.

The XRD pole figure is a convenient characterization tool to obtain average data of NW ensembles. The pole figures of a sample with as-grown GaAsSb NWs were first recorded at the Bragg angles of the 111 and 220 GaAs reflections (Dheeraj et al., 2008a). We observed a central diffraction spot in the 111 GaAs XRD pole figure pattern, corresponding to the (111) planes parallel to the surface, and additional sharp spots located at an inclination angle of 70.5° in a sixfold symmetry pattern, corresponding to the other {111} planes. In the 220 XRD pole figure, spots were located at 35.3° in a similar sixfold symmetry pattern, corresponding to {220} planes. These features confirm that the NW growth axis was aligned with the $[\bar{1}\,\bar{1}\,\bar{1}]$ GaAs direction. Both pole figures show a sixfold symmetry, which must be due to the twinning of the ZB structure in the NWs, as a pure and single ZB phase has a threefold symmetry along <111> directions. θ -2θ scans (not shown here) were performed across each spot of the pole figures and we observed that the GaAsSb diffraction peaks of crystal orientation A and B parts had equivalent intensities. This means that the average volumes of GaAsSb segments with crystal orientation A and B, respectively, in the NW ensembles are equal.

In the 220 GaAs XRD pole figure pattern, we also observed a second set of six spots corresponding to hexagonal WZ $\{11\,\bar{2}\,0\}$ planes normal to the substrate surface. It is very likely that this hexagonal phase corresponds to the bottom part of the NWs, which consists of GaAs (no Sb) base of the NW as was mentioned in the growth procedure described above. This is consistent with our observation (as mentioned earlier) that pure GaAs NWs grown under our experimental conditions adopt the WZ structure, in accordance with previous reports on MBE-grown GaAs NWs. We should mention that the GaAs NW base of the present GaAsSb NWs was not observed by TEM. During sample scratching to collect NWs on the TEM grid, the NWs were probably broken above the GaAs part of the NW.

3.2 Growth of GaAs/GaAsSb/GaAs axial heterostructured NWs

GaAs/GaAsSb/GaAs axial heterostructured NWs were grown with 20 minutes, 30 seconds and 5 minutes growth times for each respective segment. The TEM image of such NW is shown in Fig. 5. The GaAs NW segment before the GaAsSb insert exhibited a pure WZ phase with almost no stacking faults. As can be seen in Fig. 5(a) and the HRTEM image of Fig. 5(c), the transition (marked as T1) from the GaAs WZ phase to the GaAsSb ZB phase insert is very abrupt. In about 1/3 of the studied NWs, a short (<5 nm) twinned ZB transition region is observed at the start of the GaAsSb ZB insert. The second transition, from the GaAsSb ZB insert to the upper GaAs NW segment (marked as T2), is shown by HRTEM in Fig. 5(b). In most of the NWs, the defect-free GaAsSb ZB insert was directly followed by a few nanometers of a twinned GaAs cubic phase (ZB/3C). Above this microtwin, a GaAs 4H polytype phase is formed, before the GaAs NW segment again returned to a WZ phase. The length of the GaAs 4H polytype phase is varying between 20 and 40 nm depending on the NW diameter. The WZ phase of the upper GaAs NW segment contains randomly spaced stacking faults, small regions of 4H and twinned ZB, as can be

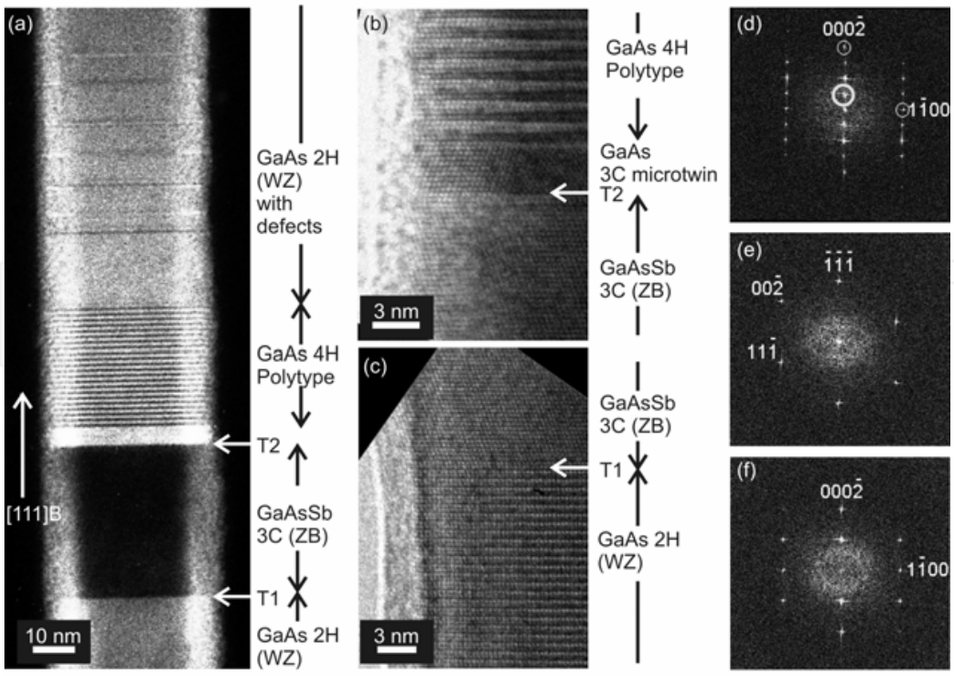

Fig. 5. Dark-field (a) and high-resolution (b, c) TEM images of a typical heterostructured GaAs/GaAsSb NW. (d), (e) and (f) are Fast Fourier Transforms (FFT) of HRTEM images of the GaAs 4H polytype above the insert, the GaAsSb ZB insert and the GaAs WZ phases below the insert, respectively (Dheeraj et al., 2008b). © 2008 American Chemical Society.

seen in Fig. 5(a). Fast Fourier transforms on HRTEM images of the 4H, ZB and WZ phases are shown in Figs. 5(d), 5(e), and 5(f), respectively. The appearance of a $1/4(0002)$ reflection in Fig. 5(d) (indicated by a thick circle) confirms a GaAs 4H polytype phase with the stacking sequence of ABCBABCB….

The 4H polytype structure is well known in bulk form in wide band gap materials such as SiC and AlN. The 4H polytype of SiC is studied in detail due to its superior electron mobility (Meyer et al., 2000). The understanding of the NW growth conditions favoring the formation of the 4H polytype in III-V materials that normally grow with a cubic ZB phase is thus an intriguing topic. The presence of a 4H polytype phase in GaAs and AlGaAs NWs was shown by Soshnikov et al., 2005. We believe that the 4H polytype is the intermediate phase between the ZB and WZ phases. As suggested by Dubrovskii et al., 2008 the gradual change in the supersaturation conditions could lead to the formation of intermediate structures such as cubic twins and a 4H polytype phase and delay the formation of the WZ phase. It is reasonable to believe that the supersaturation is gradually increasing after the shut off of the Sb flux and that this induces the 4H polytype crystal structure. However, no Sb was found above the insert, or in the gold particle by EDX, as mentioned above.

3.3 Effect of Sb on the crystal structure of NWs:

The understanding of the effect of Sb on the crystal structure of these NWs is very crucial. According to a recent model proposed by Glas et al., 2007, the crystalline structure of NWs depends on the orientational position (ZB or WZ) taken by the critical nucleus of each new monolayer. This is determined mainly by the following parameters: the stacking fault

energy in the bulk ZB phase, the energy γ_{tV}^{j} (j = ZB or WZ) of the lateral interface between the NW sidewalls and the vapor (V) phase, and the chemical potential difference (supersaturation) $\Delta\mu_{LS}$ of the liquid (L) phase with respect to the solid (S) phase. WZ formation in NWs of a given material requires two conditions: a facet energy lower for WZ than for ZB and a supersaturation $\Delta\mu_{LS}$ higher than a material-dependent critical value $\Delta\mu_c$. The latter scales with the stacking fault energy, which is about 20% higher in GaSb than in GaAs (Takeuchi & Suzuki, 1999). Moreover, according to the model of Glas et al., 2007, we expect $\Delta\mu_c$ to increase if the difference $\gamma_{tV}^{ZB} - \gamma_{tV}^{WZ}$ decreases. This difference should indeed be lower in GaAsSb, since the cohesive energy of GaSb is about 10% less than that of GaAs (Phillips, 1973). Hence, $\Delta\mu_c$ could be significantly larger in GaAsSb than in GaAs. This could be enough to offset the balance in favor of ZB nucleation in GaAsSb NWs, even if $\Delta\mu_{LS}$ does not change much. On the other hand, the addition of Sb in the vapor phase could induce a significant change of $\Delta\mu_{LS}$ in the liquid catalyst. If $\Delta\mu_{LS}$ decreases, this change would also be in favor of ZB nucleation. However, for the quaternary system (Au-Ga-As-Sb) considered here, there is no suitable thermodynamical data from which the change of $\Delta\mu_{LS}$ induced by Sb can be predicted. Therefore, at the present stage, we cannot define which phenomenon prevails to explain the ZB structure of [111]B-oriented GaAsSb NWs. It can be due to either an increase of $\Delta\mu_c$ or decrease of $\Delta\mu_{LS}$ (or both).

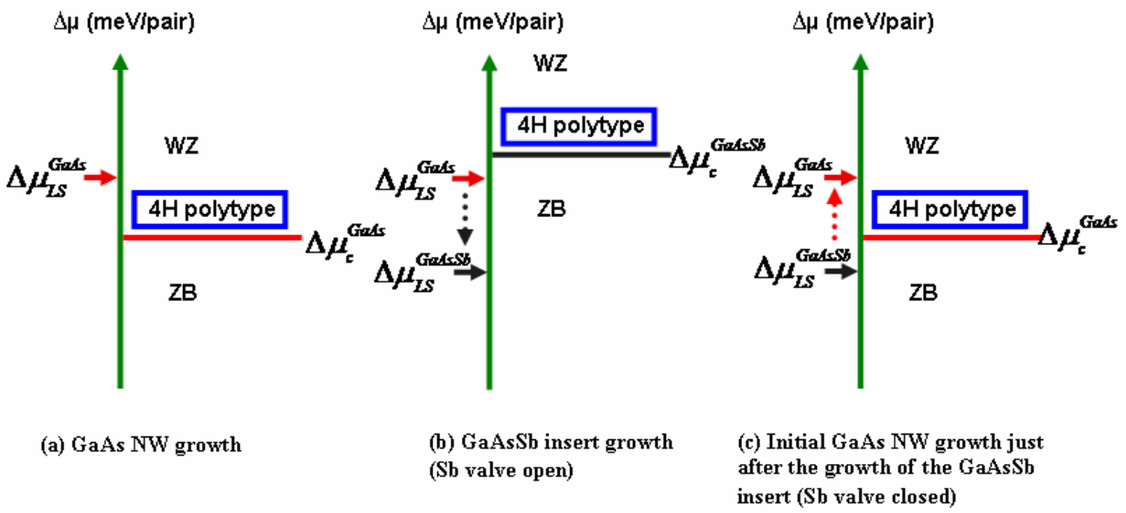

Fig. 6. Schematic illustrations of the possible configurations of the chemical potential difference $\Delta\mu_{LS}$ (red and black arrows) and material-dependent critical supersaturation $\Delta\mu_c$ (red and black horizontal lines) at different stages of NW growth (Dheeraj et al., 2008b). © 2008 American Chemical Society.

According to the HRTEM results, the most likely explanation for the phase transitions at the interfaces (T1 and T2 in Fig. 5) is that they are induced by the changing of both $\Delta\mu_c$ and $\Delta\mu_{LS}$ due to the introduction of Sb flux while growing. It should be noted that the chemical potential difference (supersaturation) $\Delta\mu_{LS}$ is gradually varying with time when the Sb flux is opened or closed, whereas the material-dependent critical supersaturation value $\Delta\mu_c$ is instantaneously changed between its corresponding values $\Delta\mu_c^{GaAsSb}$ and $\Delta\mu_c^{GaAs}$ for GaAsSb and GaAs, respectively. We believe that this is the main reason for forming two different interfaces at T1 and T2, and the detailed discussion is described in the following. According

to the NW growth models by Glas et al., 2007, and Dubrovskii et al., 2008, the supersaturation value for the Au liquid droplet ($\Delta\mu_{LS}$) required to nucleate the 4H polytype phase is higher than for the ZB phase, and the WZ phase is higher than for the 4H polytype phase, as shown in Fig. 6. As the GaAs NW grows, the chemical potential difference $\Delta\mu_{LS}$ is $\Delta\mu_{LS}^{GaAs}$ in the WZ phase region (indicated with a red arrow in Fig. 6(a)). At the start of the GaAsSb insert growth, the critical supersaturation value $\Delta\mu_c$ instantaneously increases to the value required for the formation of the GaAsSb ZB phase ($\Delta\mu_c^{GaAsSb}$) (black horizontal line in Fig. 6(b)), whereas the chemical potential difference needs some time to gradually decrease to the equilibrium condition ($\Delta\mu_{LS}^{GaAsSb}$, indicated by a black arrow in Fig. 6(b)) for the formation of the GaAsSb ZB phase. However, the NWs should have ZB phase after introducing Sb into the MBE chamber due to that $\Delta\mu_{LS} < \Delta\mu_c^{GaAsSb}$, and hence a sharp interface occurs at T1. Reversely, after turning off the Sb flux, even though $\Delta\mu_c$ instantaneously goes back to $\Delta\mu_c^{GaAs}$, as shown by the red horizontal line in Fig. 6(c), $\Delta\mu_{LS}$ is gradually increasing to the supersaturation value $\Delta\mu_{LS}^{GaAs}$. This gradual change in the supersaturation condition could lead to the formation of intermediate structures such as cubic twins and 4H polytype, and thus delay the formation of the WZ phase. This is, however, just one possible explanation for why there are two different GaAs/GaAsSb interface transitions (at T1 and T2) based on our HRTEM observations, and does not yet give a complete description of the actual variations of $\Delta\mu_{LS}$ and $\Delta\mu_c$.

3.4 Growth of GaAs NWs with multiple GaAsSb inserts

We further demonstrate the growth of GaAs NWs with 4 GaAsSb inserts at an interval of growth time of 10 minutes on GaAs(111)B substrates. More than half a dozen of NWs were investigated by TEM and a typical NW is shown in Fig. 7. We could observe only three GaAsSb inserts in a NW by TEM. We believe that the first insert could have broken during the TEM sample preparation. The average growth rates of the three GaAsSb inserts and the lengths of the GaAs segments between each insert were measured from the TEM image in Fig. 7 and the results are shown in Fig. 8. It is observed that the average growth rate for the third insert is higher than for the second insert. TEM investigation on a number of these NWs show a similar increase in growth rate from the second to the third insert, while the growth rate of the fourth insert is observed to either increase, remain constant or decrease as compared to that of the third. The same trend is observed for the GaAs segments above these inserts.

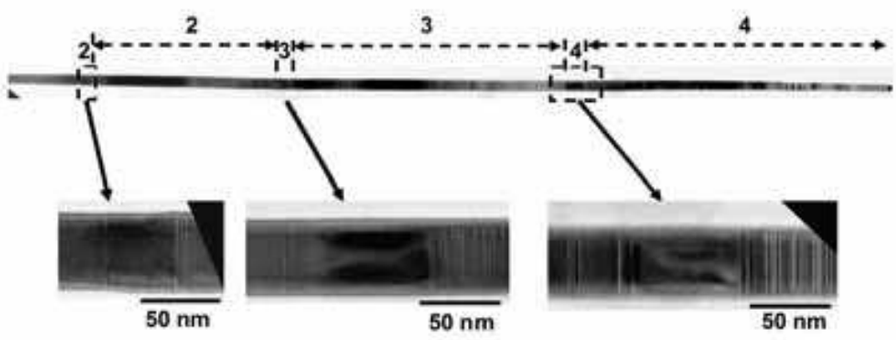

Fig. 7. (a) TEM image of a typical GaAs NW with three of four GaAsSb inserts visible (Dheeraj et al., 2009). © 2009 Elsevier.

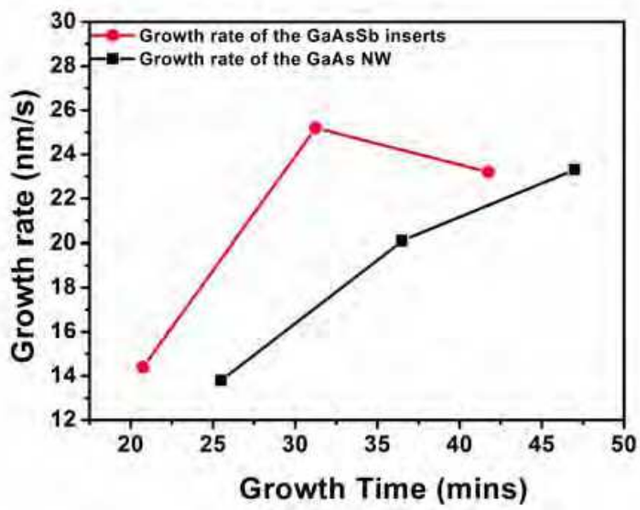

Fig. 8. Average growth rate of each GaAs segment and GaAsSb insert of the NW shown in Fig. 7 plotted versus the time at which half of the segment/insert is grown (Dheeraj et al., 2009). © 2009 Elsevier.

The crystalline structure of the GaAs segments is observed to be dominated by the WZ phase, whereas the GaAsSb inserts are observed to be of ZB phase. This result is consistent with the observations made before (Dheeraj et al., 2008a). The lower part of the GaAs NW has almost no stacking faults and the transition from the GaAs WZ phase to the GaAsSb ZB phase is always abrupt. The transition from the GaAsSb ZB phase of the first insert to the GaAs WZ phase above, however, exhibits a few nanometres of a 4H polytype phase followed by some stacking faults up to a few tens of nanometers, before maintaining pure WZ structure for a couple of hundred nanometers. This is a similar structure as depicted in Fig. 5. Further, with the increase in length of the NWs, the density of stacking faults was observed to increase in the GaAs segments. Interestingly, in spite of the higher density of stacking faults present in the upper GaAs segments, all the upper GaAsSb inserts were pure ZB without any twinning defects, and in addition the transition from the GaAs WZ phase to the GaAsSb ZB phase and vice-versa is abrupt (i.e, no 4H polytype). It is plausible that the growth rate of the NWs affects the kinetics of the change in supersaturation levels required for formation of ZB to WZ. Thus, we speculate that it is the slower growth rate near e.g. the position of the second insert that helps the formation of intermediate phases such as the GaAs 4H polytype, and as the growth rate of the NW increases, the change in supersaturation levels instead instantaneously leads to the formation of a WZ GaAs phase directly after the GaAsSb insert.

EDX investigations on the GaAsSb inserts revealed that the mole fraction of Sb was increasing with the insert's position along the NW. No significant relation between the Sb mole fraction and either the lengths of the GaAsSb inserts or the diameters of the NWs was observed. We believe the increase in Sb mole fraction with the NW length could be either due to increase in growth rate of the NW or due to decrease in the NW temperature with its length. However, further investigation is needed to clarify which mechanisms that are responsible for the change in Sb mole fraction along the NW.

3.5 Growth kinetics of GaAs NWs and the formation of stacking faults

According to the VLS growth model proposed by Dubrovskii & Sibirev 2007, the most predominant Ga adatom diffusion paths favouring the growth of NWs by MBE were considered to be (a) diffusion of Ga adatoms on the substrate surface to the NW base and (b) diffusion of Ga adatoms from the NW base to the Au droplet along the NW sidewall. Part of the Ga adatoms diffusing on the substrate could contribute to the growth of a 2D layer and part of the Ga adatoms diffusing along the NW sidewall contribute to the radial growth of the NW. We should point out here that, due to the design of the MBE growth chamber with the incident angles of molecular beams being typically 57° to the substrate surface in our case, the number of Ga adatoms hitting the NW sidewall increases proportionally to the length of the NW until shadowing from adjacent NWs sets in. This could lead to the increase in the probability of Ga adatoms either diffusing to the Au droplet or adding to the radial growth of the NW. As we hardly observed any radial growth of the NWs, an increase in axial growth rate of the NWs is quite plausible, which explains the increase in growth rate from the second to the third GaAsSb insert (and likewise for the GaAs segments above these inserts) , as was observed in the NW of Fig. 7. As mentioned above, after a certain critical average NW length, the growth rates of NWs were observed to either increase further, become constant or decrease, which we believe is dependent on the amount of shadowing of the molecular beam from adjacent NWs. The amount of shadowing, which is time-averaged due to the rotating substrate, will be different from NW to NW due to the random distribution of NW positions and the variation in length of adjacent NWs. In general, shadowing will affect the growth rate relatively more for shorter NWs than for longer NWs.

It has been shown that the WZ phase is favoured above a certain critical liquid supersaturation and that the ZB phase is prevailing below (Glas et al., 2007). The liquid supersaturation is quite sensitive to the rate of incoming adatoms to the Au droplet and to the rate of NW formation under the Au droplet, which could vary during the formation of every monolayer of the NW, leading to fluctuations in supersaturation levels. If the supersaturation is close to the critical supersaturation, these fluctuations could lead to the bistable conditions favouring both WZ and ZB phase, leading to the formation of stacking faults. The formation of the high density of stacking faults in the GaAs segment after the third and fourth GaAsSb insert could be attributed to fluctuations in the levels of supersaturation caused by turning on and off the Sb flux. However, this argument is not sufficient to explain the reason for the increase in the density of stacking faults with the length of the NW.

Cornet et al., 2007, suggested that a decrease in the rate of incoming In adatoms to the Au particle after a certain length of the InP NWs, lead to the formation of stacking faults due to the decrease in supersaturation to bistable conditions where both WZ and ZB exists. Conversely, we noticed an increase in the growth rate and density of stacking faults in GaAs NWs with its length, indicating that the formation of stacking faults is possible due to the increase in growth rate of NWs. This is further corroborated by the presence of a high density of stacking faults in the GaAs NWs grown under higher Ga flux equivalent to a nominal planar growth rate of 1.8 MLs^{-1} (not shown here). Although little can be said about the effects of increase in growth rate of NWs on change in supersaturation levels, these results suggest that the formation of stacking faults introduced in the GaAs segment after the third and fourth GaAsSb insert could be due to the coincidence of a change in supersaturation conditions by turning on and off the Sb flux and the increase in the growth

rate of the NW. These results suggest that long and defect-free WZ GaAs NWs can be obtained at a lower growth rate of NWs.

3.6 Growth of GaAs/AlGaAs radial heterostructured NWs

Here, we demonstrate the growth procedure of GaAs/AlGaAs radial heterostructured core-shell NWs, with strongly enhanced photoluminescence efficiency from the GaAs core due to the shell passivation of surface states (Zhou et al., 2009). GaAs NWs were first grown for 25 minutes in the MBE chamber at the growth conditions mentioned earlier. The growth of AlGaAs was initiated by introducing the Al flux towards the substrate by opening the shutter in front of the effusion cell. The temperature of the Al effusion cell was preset to what would yield an $Al_xGa_{1-x}As$ layer with x equal to 0.3 or 0.6 on a GaAs(001) substrate. The V/III flux ratio was kept constant for both Al fluxes used by adjusting the As_4 flux. For the (nominal) $Al_{0.3}Ga_{0.7}As$ shell samples, the shell growth times were 1 min, 5 min and 15 min, whereas for the (nominal) $Al_{0.6}Ga_{0.4}As$ shell samples, the shell growth times were 0.5 min, 2 min and 7 min. The Al, Ga and As_4 fluxes were shut down simultaneously at the end of the AlGaAs shell growth and the substrate temperature immediately ramped down to room temperature. The as-grown NWs were characterized by SEM to systematically investigate the morphology of the GaAs core NWs and GaAs/AlGaAs core-shell NWs with different growth times and Al contents. 45°-tilted view SEM images of the GaAs core NWs and the GaAs/AlGaAs core-shell NWs are shown in Figs. 9 (a-c). For determination of the geometric sizes of the as-grown NWs, 40 NWs for each growth condition were randomly chosen from the SEM images.

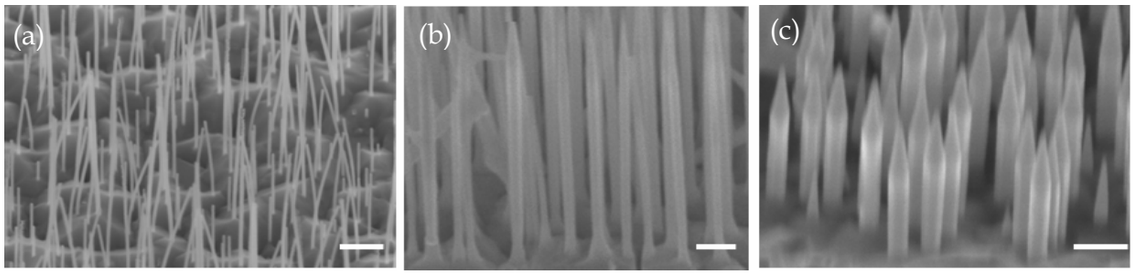

Fig. 9. 45°-tilted SEM images of the GaAs core NWs grown for 20 min (a), with $Al_{0.3}Ga_{0.7}As$ shell grown for 15 min (b), and with $Al_{0.6}Ga_{0.4}As$ shells grown for 7 min (c). Scale bar is 200 nm (Zhou et al., 2009).

The GaAs core NWs grew predominantly perpendicular to the substrate surface ([111]B direction) with a constant diameter over its length. The length of the NW is defined from the GaAs surface of the buffer to the tip of the NW. The diameters of the GaAs core NWs are varying from 10 nm to 25 nm and the lengths of the NWs are ranging from 240 nm to about 1.2 μm. The lengths of the GaAs core NWs were observed to decrease with increasing diameter. It confirms that growth of the NWs is fed by diffusion of adatoms from the surface of the substrate and/or from the sidewalls to the Au droplet at top of the NWs, as described by Dubrovskii & Sibirev, 2007. However, this behavior did not retain after the initiation of AlGaAs shell growth, which could be due to the deposition of Ga and Al adatoms directly on the NW sidewalls by a vapor solid (VS) growth mechanism.

No tapering was observed in any of the investigated GaAs NWs, whereas tapering was observed in the GaAs/AlGaAs core-shell NWs. Tapering is often observed when the length

of the NWs exceeds the diffusion length of group III adatoms impinging on the NW sidewall as mentioned in 1.1. It is well known that Al is very reactive. Consequently, the effective surface diffusion barrier is higher for Al adatoms (~1.74 eV for AlAs grown on AlAs (001)) than for Ga adatoms (~1.58 eV for GaAs grown on GaAs (001)) (Shitara et al., 1993). This results in a shorter adatom diffusion length for Al compared to Ga, whereby radial sidewall deposition becomes more pronounced leading to a tapered morphology for GaAs/AlGaAs core-shell NWs. The tapering of the core-shell NWs becomes much more pronounced with increasing shell growth time and higher Al content. Also, we observed that both the mean diameter and the mean length of the NWs are increasing with increasing shell growth time, which shows that the AlGaAs shell grows in both axial and radial directions.

Comparing the $Al_{0.3}Ga_{0.7}As$ and $Al_{0.6}Ga_{0.4}As$ shell growth, we find an increasing radial and a decreasing axial growth rate of the AlGaAs shell with an increased Al content. At the same time, the mean volume of the GaAs/AlGaAs core-shell NWs quickly increases when the AlGaAs shell is formed, e.g. about 90 and 60 times for samples with 30% Al and 60% Al, respectively, compared to the mean volume of the NWs without AlGaAs shell. This is consistent with an observed decrease in the growth rate of the 2D layer with increase in shell growth time, where the 2D layer height is measured by the distance between the $Al_{0.3}Ga_{0.7}As$ marker layer in the buffer and the top surface of the sample in the cross-sectional SEM image.

The observed rapid increase of the NW volume with the AlGaAs growth time could be due to the shorter diffusion length of the Al adatoms as well as to the increasing collection area of the sidewalls of NWs with the increasing shell growth time. NWs collect Ga and Al adatoms in three different ways; (1) diffusion from the substrate surface, (2) direct impingement on the NW sidewalls, and (3) direct impingement on the gold droplet. A larger area of the NW sidewalls (effective collection area = *length* × *diameter*) is obtained when NWs get longer, whereby the NWs can collect more Al and Ga adatoms. At the same time, the shorter diffusion length of the Al also contributes to trap more and more Al and Ga adatoms migrating on the sidewalls of the NWs. Both of these two factors enhance each other, which results in a very fast increase of the NW volume. After the AlGaAs shells start to grow, the total flux impinging on the sample surface should remain constant. The AlGaAs either deposits on the NWs or on the substrate surface. Once NWs can capture more AlGaAs with a larger area of NW sidewalls, a slower growth rate of the 2D layer should be expected. A decrease in the growth rate of the 2D layer with the increase in growth time of the AlGaAs shell is also indeed what is observed (Zhou et al., 2009).

Finally, lower density of NWs was also found with increasing AlGaAs shell growth time, e.g. it is about 90 NWs/μm^2 for the GaAs core NW sample and roughly 50 NWs/μm^2 for the sample with $Al_{0.3}Ga_{0.7}As$ shell grown for 15 minutes. When the AlGaAs growth takes place, there is a possibility that some of the shorter NWs (e.g. the GaAs core NWs ~250 nm) might be buried by the 2D layer at the AlGaAs shell growth stage. We observed that both the radial growth rate of the AlGaAs NW shell and the growth rate of 2D AlGaAs increase with increased Al flux, whereas the NW axial AlGaAs growth rate is not significantly changed for average size NWs. The ratio between the NW axial AlGaAs growth rate and the 2D AlGaAs growth rate, of importance for NW burial, thus reduces with increase in Al flux. The ratio will be even further reduced for shorter NWs by the fact that shorter GaAs/AlGaAs core-shell NWs will get less Ga and/or Al adatoms compared to longer NWs due to both the smaller sidewall collection area and the shadowing effect. The shadowing effect is induced

by the inclined molecular beam with respect to the substrate normal (here ~37°). Due to this effect, shorter NWs will be shadowed by longer neighboring NWs, which will also lead to a reduced growth rate. Shorter NWs may therefore be completely buried by the 2D layer, leading to a decrease in NW density.

Fig. 10(a) shows the [110] zone axis HRTEM image of a typical GaAs core NW (14 nm diameter). A HRTEM image of a typical GaAs/AlGaAs core-shell NW ($Al_{0.3}Ga_{0.7}As$ shell grown for 15 minutes) is shown in Fig. 10(b). SAED patterns in Fig. 10(a) and 10(b) reveal a wurtzite (WZ) crystal structure both in the GaAs core and in the AlGaAs shell. By comparing the HRTEM (Fig. 10(c)) and scanning-TEM images (Zhou et al., 2009) of the same NW, it indicates that apart from radial AlGaAs growth, an axial AlGaAs is also grown on top of the GaAs core. It can also be seen from HRTEM image (Fig. 10(c)), that stacking faults appear at the region where the axial AlGaAs starts to grow (by VLS) on top of the GaAs core. At the same time, it also shows that the radial AlGaAs shell exactly follows the crystal structure (including stacking faults) of the GaAs core. The interface between the GaAs core and the radial AlGaAs shell is relatively sharp and the thickness of the radial shell along the NW axis is highly uniform until the tapered AlGaAs NW region at the top. We have no indication that Al is diffusing into the GaAs NW core for neither of the two studied shell compositions. For the core-shell NW shown in Fig. 10(b) ($Al_{0.3}Ga_{0.7}As$ shell grown for 15 minutes), the diameter of the GaAs NW core is ~15 nm and for the whole core-shell NW ~ 60 nm, which is consistent with the observations from SEM.

In addition, a high angle annular dark field STEM characterization performed on these NWs (see Zhou et al., 2009) revealed that the AlGaAs NW grown on the top of the GaAs NW is a long (~ 800 nm) AlGaAs "core" with a radial AlGaAs "shell", with different Al compositions in the "core" and "shell", respectively. The observation of forming self organized core-shell structures is consistent with previous published results by Chen et al., 2007.

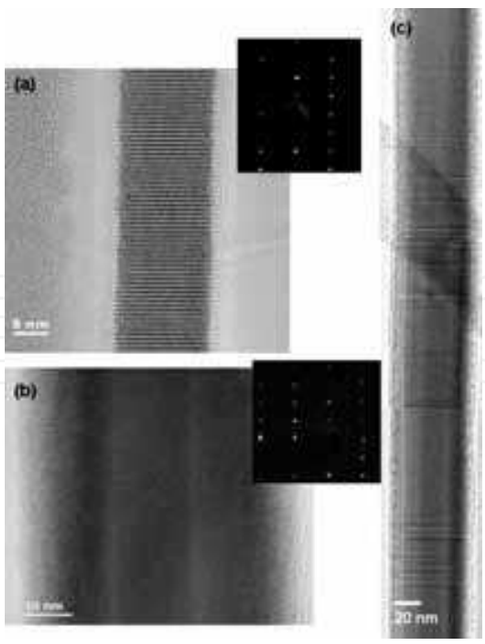

Fig. 10. HRTEM images of (a) GaAs core and (b), and (c) a typical GaAs/$Al_{0.3}Ga_{0.7}As$ core-shell NW, together with the selected area electron diffraction patterns (inset of image (a) and (b) (Zhou et al., 2009).

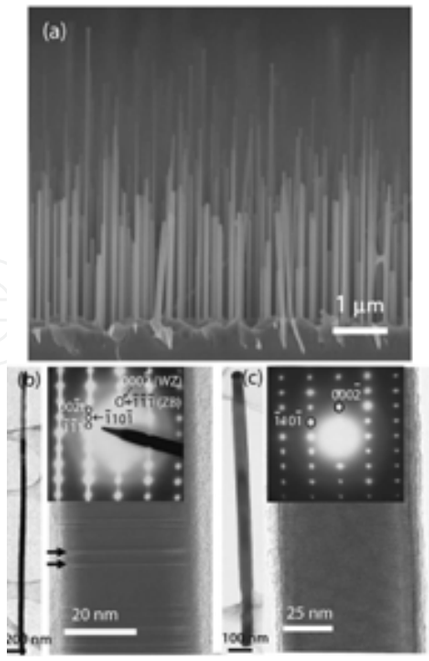

Fig. 11. a) Side view SEM image of the as-grown GaAs NWs. TEM (left) and HRTEM (right) image of a GaAs NW with (b) and without (c) stacking faults (Hoang et al., 2009). © 2009 American Institute of Physics.

3.7 Band gap of WZ GaAs

The newly observed WZ phase of the GaAs NWs raises questions about fundamental physical parameters such as the band gap energy, exciton binding energy, carrier effective masses and phonon energies. As mentioned earlier, it is necessary to grow the NWs without any stacking faults to determine the bandgap energy of WZ material. The SEM image of the GaAs NWs shown in Fig. 11 (a) depicts that there are two typical sets of wires: short wires (~ 2 μm, and large diameter ~ 60 nm) and long wires (~ 4 μm, and smaller diameter ~ 30-40 nm). This is in agreement with the model proposed by Dubrovskii & Sibirev, 2007, which shows that the NWs with smaller diameter grow faster than NWs with large diameter at the same flux.

From HRTEM characterization, it appears that the narrow and long NWs are associated with stacking faults while the wide and short NWs are free of stacking faults. These observations are in agreement with our previous report where we attributed the formation of stacking faults to the faster growth rate of NWs (Dheeraj et al., 2009). Figs. 11(b) and 11(c) show TEM images of a GaAs NW with and without stacking faults, respectively. The right panel in Fig. 11(b) shows a magnified image of a small portion of the same NW shown in the left panel with clear appearance of stacking faults and is complemented with the electron diffraction pattern shown in the inset of Fig. 11(b). The right panel in Fig. 11(c) shows a magnified image of the stacking fault free NW, indicating a pure WZ crystal structure for this NW. From the TEM images of these two representative NWs and several others studied, we conclude that narrow (and long) NWs appear to have a low density of stacking faults associated with short ZB segments (~ 2 nm) sandwiched in between a dominating WZ structures while wide (and short) NWs show a pure WZ crystal structure free of stacking faults or ZB segments.

Low temperature μ-PL measurements from single WZ GaAs NWs show a PL emission band at an energy of ~ 29 meV higher in comparison with the ZB GaAs free exciton emission energy (1.515 eV). Some NWs exhibited PL emissions from both ZB and WZ phases, at ~1.515 and 1.544 eV, respectively. The results are consistent with the HRTEM observation that short ZB segments appear in the GaAs NWs that contain stacking faults.

Fig. 12 shows PL spectra from four single WZ GaAs NWs at 4.4 K. The 633 nm cw excitation laser was defocused (spot size ~ 5 μm) so that individual NWs were entirely excited. The PL emissions from all these NWs exhibited strong emission bands centered at ~ 1.535 eV. The PL spectra display a broad emission range with several features which we now discuss in detail. All NWs (wires 1 - 4) show an emission peak at 1.544 eV (in wire 2 the peak appears as a shoulder), 29 meV higher in comparison with the ZB GaAs free exciton emission energy (1.515 eV). We suggest that this is the free exciton emission for WZ GaAs. There exist a few recent results on the PL emission for WZ GaAs nanostructures but the results are inconsistent. Martelli et al., 2007, reported the free exciton emission peak in WZ GaAs NWs to be at an energy 7 meV higher compared with the ZB GaAs free exciton energy, while Moewe et al., 2008, reported a 10 meV lower energy for WZ GaAs nano-needles. Our result (~ 29 meV higher), however, is close to the results reported in some earlier theoretical works (Mujica et al., 1995; Murayama & Nakayama, 1994; Yeh et al., 1992) where the WZ GaAs band gap energy was predicted to be ~ 30 - 33 meV higher than for ZB GaAs.

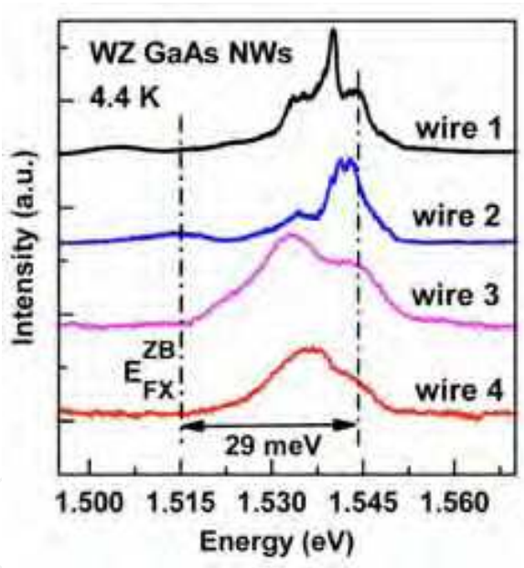

Fig. 12. μ-PL spectra from four different NWs labeled 1-4 (Hoang et al., 2009). © 2009 American Institute of Physics.

Wires 1 and 2 exhibit narrow emission lines at ~ 1.54 eV, while a broader peak at lower energy (~ 1.532 eV) is observed in all wires 1 – 4. The origin of these emission bands are not clear at the moment, but the emissions most probably result from excitons bound to defects such as morphological irregularities or are impurity related. We note that in the PL spectra of wires 1 and 2 there are also emission peaks at 1.505 and 1.515 eV, respectively. These peaks are close to the exciton emission energies in ZB GaAs NWs (Titova et al., 2006). However, in wires 3 and 4, there are no indications of emission in this energy range. We suggest that these weak emissions are associated with the ZB GaAs segments that are

observed in the WZ GaAs NWs with stacking faults. Again, this result is consistent with HRTEM results shown in Figs. 11 (b) and (c), where some GaAs NWs exhibit pure WZ free of stacking faults (and ZB segments), while other NWs exhibit a low density of stacking faults, which inherently possesses ZB phase.

In order to gain further insight of the observed emission peaks from these WZ GaAs NWs, we have measured the temperature dependence of the PL spectra of wire 1 from 4.4 K to 70 K. Several observations were obtained from the temperature dependence of the various peaks. The sharp emission peak at 1.54 eV (labeled 2) dominates at low temperature while the GaAs WZ free exciton emission peak (labeled 1) only appears as a shoulder. As the temperature increases, the sharp peak (2) decreases in intensity and disappears by 40 K, above which only the free exciton emission peak remains.

The temperature dependence of the emission energies of peaks 1 and 2 is plotted in Fig. 13, and is compared with the emission energy of a ZB GaAs/AlGaAs core-shell NW as reported by Titova et al., 2006. The solid lines are fits to the data of peaks 1 and 2 as well as the ZB NWs from Titova et al., 2006, using a modified form of the Varshni equation (Cardona et al., 2004). We note that the emission energies of the WZ free exciton (peak 1) and defect-related (peak 2) peaks have a similar temperature dependence as the exciton emission energy of the ZB GaAs NW. The defect-related emission energy closely follows the free exciton energy and quenches at ~ 40 K, suggesting that the emissions are not related to deep levels but are rather excitonic in nature.

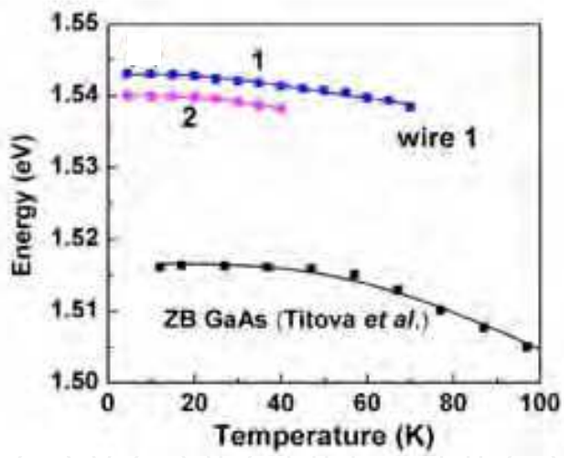

Fig. 13. PL energies of peaks 1 and 2 (see text) as a function of temperature (Hoang et al., 2009). © 2009 American Institute of Physics.

Hence, we conclude that PL measurements on single NWs at low temperatures reveal a peak related to the WZ GaAs free exciton emission at an energy ~ 29 meV higher in comparison with the free exciton emission energy in ZB GaAs. The WZ/ZB GaAs band alignment is believed to be type II with the ZB conduction band edge energy lower than for WZ, in which case PL emission can be expected anywhere in the energy range from the WZ GaAs band gap to even below the ZB GaAs band gap depending on the density, size and distribution of the ZB segments. Our observation of weak emission peaks at energies close to the free exciton energy in ZB GaAs for some NWs, in combination with our HRTEM images of some of the WZ NWs where stacking faults (inherently possessing ZB phase) are observed, corroborates this view.

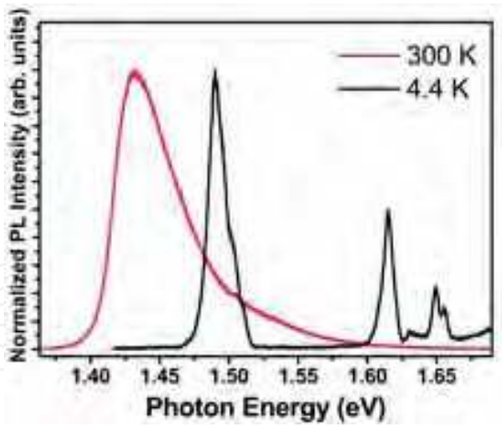

Fig. 14. Room and low (4.4 K) temperature μ-PL emission spectra from a single GaAs/AlGaAs core-shell NW (Zhou et al., 2009).

3.8 Optical properties of GaAs/AlGaAs core-shell NWs

Fig. 14 shows RT and low temperature (4.4 K) μ-PL emission spectra from the same GaAs/$Al_{0.3}Ga_{0.7}As$ core–shell NW. For the investigated bare GaAs core NWs, there is no detectable PL signal at RT. The RT spectrum of the core-shell NW shows only GaAs related emission at 1.431 eV (full width at half maximum (FWHM) is ~49 meV). In contrast, at 4.4 K, the spectrum of the core-shell NW shows both GaAs emission at 1.489 eV (FWHM is ~12 meV) and several PL peaks above 1.6 eV.

We note here that the emission energy (1.489 eV) for the GaAs core is lower than the free exciton energy (1.515 eV) of ZB GaAs. This is probably due to the recombination from the type II band alignment that can occur due to stacking fault created GaAs ZB segments sandwiched in between a dominating GaAs WZ structure (Pemasiri et al., 2009; Hoang et al., 2009). It is important to note that no PL emission was observed from bare GaAs core NWs at RT. As has already been reported by several authors (Titova et al., 2006; Chen et al., 2007), the shell in the GaAs/AlGaAs core–shell NW helps to increase the radiative recombination efficiency by approximately two orders of magnitude through the suppression of non-radiative surface recombination at the GaAs surface. As can be seen in Fig. 14, PL emissions from both GaAs and AlGaAs are observed at low temperature.

The PL peaks above 1.6 eV are most likely related to recombination from carriers localized in the AlGaAs region (~1 μm) at the top of the NW. The occurrence of several PL peaks is believed to be due to some local composition variations (10–15%) in this AlGaAs region. It has already been reported that for the axial VLS growth of AlGaAs on top of GaAs, a self-formed AlGaAs core–shell structure is formed with a radial variation in the Al composition (Chen et al., 2007). The existence of AlGaAs related PL peaks from the GaAs/AlGaAs core–shell NWs suggests that there is room for improvement of the growth, especially by reducing the axial growth of AlGaAs

3.9 Optical properties of GaAs/AlGaAs core-shell NWs with GaAsSb insert

The GaAs/GaAsSb/GaAs axial heterostructured NWs are very interesting due to that band-structure in these materials is engineered not just by changing the crystal material but also by the crystal phase. Here, we show that the crystal structure of the GaAs barrier on the upper interface of GaAsSb insert can be altered by introducing a growth interruption (GI)

immediately after the growth of the GaAsSb insert. The optical properties of such structures are discussed. In addition, these NW have a AlGaAs shell as discussed in 3.7.
Fig. 15 (a) shows the dark field TEM image of a GaAs/AlGaAs core-shell NW with a GaAsSb insert where no GI was employed after insert growth. The GaAsSb insert has a ZB crystal structure, whereas the GaAs core has WZ crystal structure. The AlGaAs shell copies the crystal structure of the WZ or ZB core as discussed before. HRTEM images of the top and bottom GaAs/GaAsSb interfaces are shown in Fig. 15(b) and (c), respectively. Due to the absence of the GI in this NW, a ZB GaAs segment (~5 nm) appears after the growth of the GaAsSb insert, denoted by a double headed arrow in Fig. 15(b). In Fig. 16(a), the PL emission from a single GaAs/AlGaAs core-shell NW with a GaAsSb insert is shown. The μ-PL emission peak related to the GaAsSb insert is observed at ~1.27 eV. The ZB segment in the GaAs barrier at the top interface of the GaAsSb insert causes a type II band alignment. This results in the spatial separation of electrons and holes in the adjacent ZB GaAs and ZB GaAsSb layers, respectively. Fig. 16(b) shows the power dependent spectra from the GaAsSb related peak at 1.27 eV. With an increase of the excitation power with a factor of ten the PL emission is broadened and the PL peak is blue shifted ~100 meV.

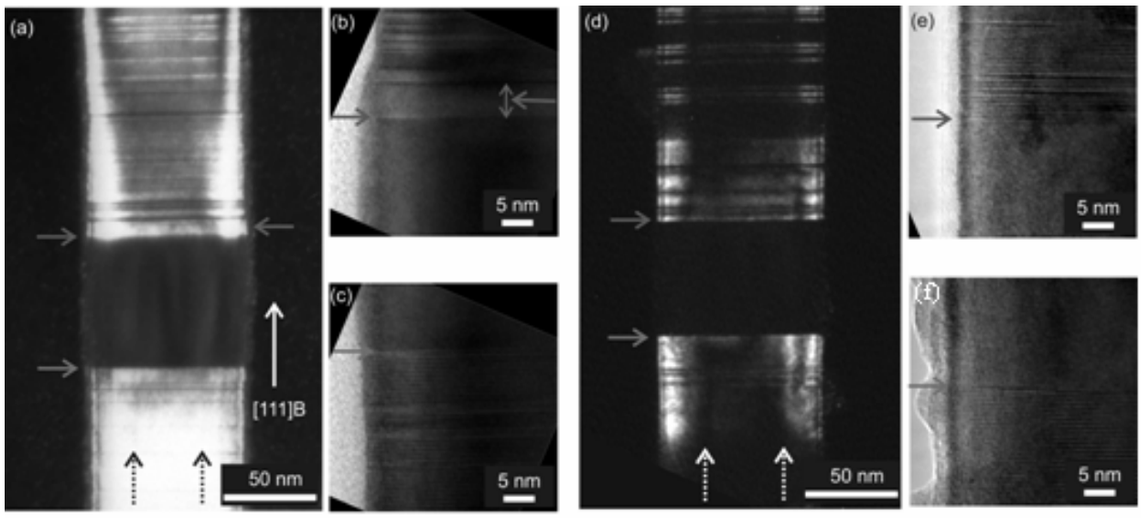

Fig. 15. Dark field TEM of a WZ GaAs/AlGaAs core-shell NW with ZB GaAsSb insert without (a) and with (d) GI, with dotted black/white arrows indicating core size. HRTEM image of (b,e) the top and (c,f) the bottom interface of the GaAsSb insert in Fig. (a,d) respectively. Arrow pointing to the left indicates ZB GaAs segment. Arrows pointing to the right indicate GaAsSb/GaAs interfaces (Moses et al., 2009). Arrows pointing to the left indicate a twin.

The large blue shift can be attributed to the band filling and band bending effect as the excitation intensity increases (Chiu et al., 2002; Dinu et al., 2003). The spatially separated electrons and holes create an electric field at the GaAsSb/GaAs interface that results in band bending as the excitation density increases. The broadening of the PL peak at higher excitation intensities is probably due to the electron state filling in the ZB GaAs segment.
A dark field TEM image of a GaAs/AlGaAs core-shell NW with GaAsSb insert where GI after the growth of GaAsSb insert is employed is shown in Fig. 15 (d). The HRTEM images

of the top and bottom GaAs/GaAsSb interfaces are shown is Fig. 15 (e) and (f), respectively. By GI, the formation of ZB GaAs segment at the upper interface of the GaAsSb insert can be avoided, which can be observed in Fig. 15(e). Hence the ZB GaAsSb insert has a well defined WZ GaAs barrier on both the interfaces. However, the WZ GaAs barrier above the GaAsSb insert has some stacking faults, the density of which is less when compared to the sample grown without GI.

In Fig. 17(a), PL emission from a single GaAs/AlGaAs core-shell NW with GI after the GaAsSb insert growth is shown. The GaAsSb related PL emission peak is observed at ~1.39

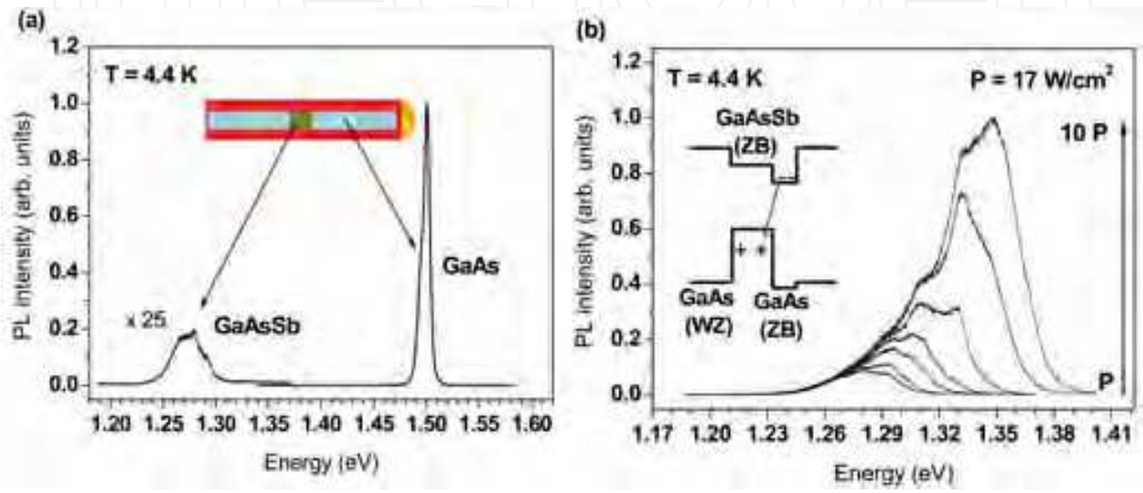

Fig. 16. (a) PL spectrum from a single GaAs/AlGaAs core-shell NW without GI after the GaAsSb insert. (b) Power dependent spectra from the GaAsSb related PL peak. Inset shows schematically the type II band alignment when the upper GaAs barrier contains a few nm thin ZB GaAs segment (Moses et al., 2009).

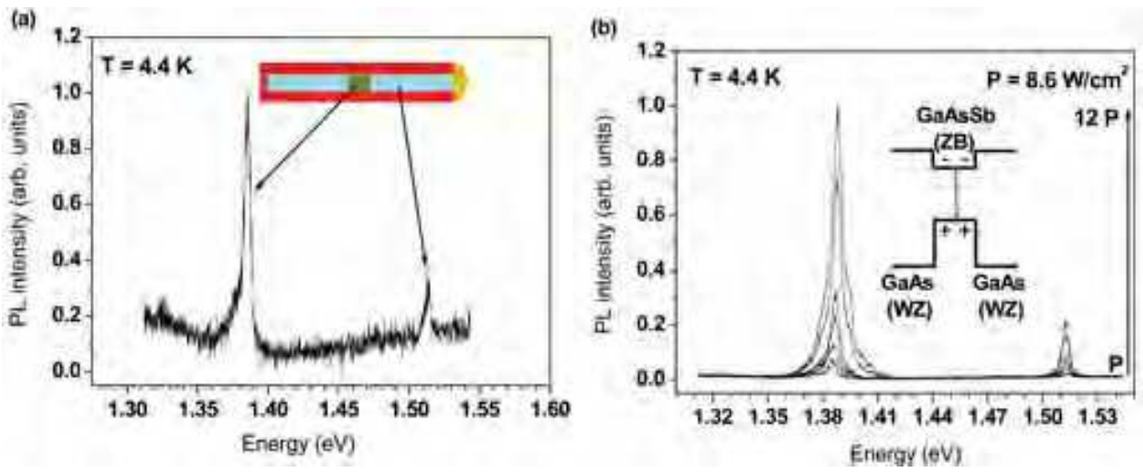

Fig. 17. (a) PL spectrum from a single GaAs/AlGaAs core-shell NW with GI after the GaAsSb insert. (b) Power dependent spectra of a GaAs/AlGaAs core-shell NW with GI after the GaAsSb insert. Inset shows schematically the type I band alignment and recombination therein (Moses et al., 2009).

eV. The WZ GaAs barriers in the GaAs/AlGaAs core-shell NW with GaAsSb insert will lead to a weak type I band alignment with both electrons and holes confined in the GaAsSb core-insert. In Fig. 17(b), the power dependent spectra of a single GaAs/AlGaAs core-shell NW with GI after the GaAsSb insert growth are shown. There is a small blue shift (~2 meV) of the GaAsSb related PL peak as the excitation intensity increases.
The power dependent PL spectra of this NW are dramatically different from the GaAsSb core-insert NW that contains a thin ZB GaAs segment at the upper GaAs/GaAsSb interface (Fig. 16(b)). We believe this is a strong indication that a type I band alignment has been achieved around the ZB GaAsSb insert with a WZ GaAs barrier at both GaAs/GaAsSb interfaces.
In all NW samples, the GaAs related PL emission is observed at ~1.50-1.52 eV, well below the free exciton PL emission observed in stacking fault free WZ GaAs NWs. This lower value is typical for WZ GaAs NWs that contain stacking faults and short ZB segments. This gives rise to type II PL emission where the stacking faults and short ZB GaAs segments act as electron traps as dicussed in 3.7.

4. Conclusions

We have demonstrated the MBE growth of ZB structured GaAsSb NWs, WZ GaAs NWs with single and multiple ZB GaAsSb inserts, and AlGaAs shells around such NWs. HRTEM studies show the GaAsSb inserts to be defect free displaying a ZB phase. Also, the crystal phase transition was observed to be abrupt at the WZ GaAs to ZB GaAsSb lower interface, whereas an intermediate 4H polytype phase was observed in the GaAs segment above the GaAsSb upper interface. We suggest that the formation of ZB GaAsSb could be due to either an increase of the material-dependent critical supersaturation value $\Delta\mu_c$ or a decrease of the supersaturation $\Delta\mu_{LS}$ in the Au particle (or both).
We showed that the growth rate of NWs in MBE increases with NW length, due to the increase in NW sidewall area (i.e. the increase in sidewall collection area for the incoming molecular beam). After a certain critical average NW length, the growth rates of NWs were observed to either increase further, become constant or decrease, which we believe is dependent on the amount of shadowing of the molecular beam on a NW from its adjacent NWs. Further, the density of stacking faults in the WZ GaAs NWs is found to be dependent on the growth rate of the NWs. These results suggest that the formation of stacking faults can be minimized by decreasing the growth rate of the GaAs NWs.
We have demonstrated the growth of stacking fault-free WZ GaAs NWs and determined the free exciton emission energy. PL measurements on single NWs at low temperatures reveal a peak related to the WZ GaAs free exciton emission at an energy ~ 30 meV higher in comparison with the free exciton emission energy in ZB GaAs. Further, we have shown the importance of AlGaAs shell to increase the radiative recombination efficiency through the suppression of non-radiative surface recombination at the GaAs surface.
Finally, we have characterized GaAs/AlGaAs core-shell NWs with a single GaAsSb insert grown without/with growth interruption (GI) after the GaAsSb insert, with ZB and WZ GaAs barrier, respectively, at the top interface of the GaAsSb insert. GaAsSb heterostructure with either ZB GaAs or WZ GaAs is believed to exhibit type II or type I band-alignment, respectively. We confirmed this by performing power dependent PL measurements, which

show a strong (~100 meV) or a weak (~2 meV) blue shift in the samples grown without or with GI, respectively. We attributed the strong blue shift and line width broadening to band bending and band filling due to a type II band alignment; while the weak blue shift is attributed to a type I band alignment. The band alignment is depending on controllable crystal phase variations in the NW and opens up new possibilities for band structure engineering of NWs.

5. Acknowledgements

The authors would like to thank J.C. Harmand, G. Patriarche, F. Glas, and L. Largeau for many fruitful discussions. The authors would also like to thank G. Patriarche and L. Largeau for their help with some of the TEM, and XRD pole figure measurements. Part of this work was supported by the 'NANOMAT' program (Grant No. 182091) and the Norwegian-French 'AURORA' program (Grant No. 187692) of the Research Council of Norway.

6. References

Agarwal, R. & Lieber, C.M. (2006). Semiconductor nanowires: optics and optoelectronics *Appl. Phys. A: Mat. Sci. Processing*, 85, 209-215.

Agarwal, R. (2008). Heterointerfaces in semiconductor nanowires. *Small*, 4, 1872-1893.

Akiyama, T.; Sano, K.; Nakamura, K & Ito, T. (2006). An empirical potential approach to wurtzite–zinc-blende polytypism in group III–V semiconductor nanowires, *Jap. J. Appl. Phys.*, 45, L275 – L278.

Algra R.E.; Verheijen, M.A.; Borgström, M.T.; Feiner, L.F.; Immink, G.; van Enckevort, W.J.P.; Vlieg, E. & Bakkers, E.P.A.M. (2008). Twinning superlattices in indium phosphide nanowires *Nature,* 456, 369.

Bernstein, R.W.; Borg, A.; Husby, H.; Fimland, B.O. & Grepstad, J.K. (1992). Capping and decapping of MBE grown GaAs(001), $Al_{0.5}Ga_{0.5}As$(001), and AlAs(001) investigated with ASP, PES, LEED, and RHEED, *Appl. Surf. Sci.,* 56-58, 74-80.

Cardona, M.; Meyer, T.; & Thewalt, M. (2004). Temperature dependence of the energy gap of semiconductors in the low-temperature limit, *Phys. Rev. Lett.*, 92, 196403.

Caroff, P.; Dick, K.A.; Johansson, J.; Messing, M.E.; Deppert, K. & Samuelson, L. (2009). Controlled polytypic and twin-plane superlattices in III-V nanowires, *Nat. Nanotechnology,* 4, 50-55.

Chen, C.; Plante, M. C.; Fradin, C. & LaPierre, R. R. (2006). Layer-by-layer and step-flow growth mechanisms in GaAsP/GaP nanowire heterostructures, *J. Mat. Res.*, 21, 2801-2809.

Chen, C.; Shehata, S.; Fradin, C.; LaPierre, R.; Couteau, C. & Gregor, W. (2007). Self-directed growth of AlGaAs core-shell nanowires for visible light applications, *Nano Lett.,* 7, 2584-2589.

Chiu, Y.S.; Ya, M.H.; Su, W.S. & Chen, Y.F. (2002). Properties of photoluminescence in type-II GaAsSb/GaAs multiple quantum wells, *J. Appl. Phys.,* 92, 5810-5813.

Cirlin, G. E.; Dubrovski, V. G.; Sibirev, N. V.; Soshnikov, I. P.; Samsonenko, Y.B.; Tonkikh, A. A. & Ustinov, V. M. (2005).The diffusion mechanism in the formation of GaAs

and AlGaAs nanowhiskers during the process of molecular-beam epitaxy, *Semiconductors*, 39, 557–564.

Cornet, D.M. & LaPierre, R.R. (2007a). InGaAs/InP core-shell and axial heterostructure nanowires, *Nanotechnology,* 18, 385305.

Cornet, D. M.; Mazzetti, V.G.M. & LaPierre, R. R. (2007b). Onset of stacking faults in InP nanowires grown by gas source molecular beam epitaxy *Appl. Phys. Lett.*, 90, 013116.

Czban, J.A.; Thompson, D.A. & LaPierre, R. (2009). GaAs core−shell nanowires for photovoltaic applications. *Nano Lett.*, 9, 148-154.

Dheeraj, D.L.; Patriarche, G.; Largeau, L.; Zhou, H.L.; van Helvoort, A.T.J.; Glas, F.; Harmand, J.C.; Fimland, B.O. & Weman, H. (2008a). Zinc blende GaAsSb nanowires grown by molecular beam epitaxy, *Nanotechnology,* 19, 275 605.

Dheeraj, D.L.; Patriarche, G.; Zhou, H.; Hoang, T.B.; Moses, A.F.; Grønsberg, S.; van Helvoort, A.T.J.; Fimland, B.O. & Weman, H. (2008b). Growth and characterization of wurtzite GaAs nanowires with defect-free zinc blende GaAsSb inserts, *Nano Lett.* 8, 4459-4463.

Dheeraj, D.L.; Patriarche, G.; Zhou, H.; Harmand, J.C.; Weman, H. & B.O. Fimland, (2009). Growth and structural characterization of GaAs/GaAsSb axial heterostructured NWs, *J. Crystal Growth,* 311, 1847-1850.

Dinu, M.; Cunningham, J.E.; Quochi, F. & Shah, J. (2003). Optical properties of strained antimonide-based heterostructures, *J. Appl. Phys.,* 94, 1506-1512.

Duan, X.; Huang, Y.; Agarwal, R.; & Lieber, C.M. (2003). Single-nanowire electrically driven lasers, *Nature,* 421, 241-245.

Dubrovskii, V.G.; Cirlin, G.E.; Soshnikov, I.P.; Tonkikh, A.A.; Sibirev, N.V.; Samsonenko, Y.B. & Ustinov, V.M. (2005). Diffusion-induced growth of GaAs nanowhiskers during molecular beam epitaxy: Theory and experiment, *Phys. Rev. B*, 71, 205325.

Dubrovskii, V.G. & Sibirev, N.V. (2007). General form of the dependence of nanowire growth rate on the nanowire radius, *J. Cryst. Growth,* 304, 504-513.

Dubrovskii, V.G. & Sibirev, N.V. (2008). Growth thermodynamics of nanowires and its application to polytypism of zinc blende III-V nanowires, *Phys. Rev. B*, 77, 035414.

Fontcuberta i Morral, A.; Spirkoska, D.; Arbiol, J.; Heigoldt, M.; Ramon Morante, J. & Abstreiter, G. (2008). Prismatic quantum heterostructures synthesized on molecular-beam epitaxy GaAs nanowires, *Small*, 4, 899-903.

Givargizov, E.I. (1975). Fundamental aspects of VLS growth, *J. Cryst. Growth,* 31, 20-30.

Glas, F.; Harmand, J.C. & Patriarche, G. (2007). Why does wurtzite form in nanowires of III-V zinc blende semiconductors? *Phys. Rev. Lett.,* 99, 146101.

Guo, Y.N.; Zou, J.; Paladugu, M.; Wang, H.; Gao, Q.; Tan, H.H.; & Jagadish, C. (2006). Structural characteristics of GaSb/GaAs nanowire heterostructures grown by metal-organic chemical vapor deposition. *Appl. Phys. Lett.,* 89, 231917.

Harmand, J.C.; Tchernycheva,M.; Patriarche, G.; Travers, L.; Glas, F. & Cirlin, G. (2007). GaAs nanowires formed by Au-assisted molecular beam epitaxy: Effect of growth temperature, *J. Cryst. Growth*, 301–302, 853–856.

Harmand, J. C.; Patriarche, G.; Péré-Laperne, N.; Mérat-Combes, M.N. ; Travers, L.; & Glas, F. (2005) Analysis of vapor-liquid-solid mechanism in Au-assisted GaAs nanowire growth, *Appl. Phys. Lett.* 87, 203101.

Hoang, T. B.; Moses, A.F.; Zhou, H.L.; Dheeraj, D.L.; Fimland, B.O. & Weman, H. (2009). Observation of free excition photoluminescence emission from single wurtzite GaAs nanowires, *Appl. Phys. Lett.,* 94, 133105.

Ihn, S.G.; Song, J.I.; Kim, T.W.; Leem, D.S.; Lee, T.; Lee, S.G.; Kooh, E.K. & Song, K. (2007). Morphology- and orientation-controlled gallium arsenide nanowires on silicon substrates *Nano Lett.,* 7, 39-44.

Ihn, S.G. & Song, J.I. (2007). InAs nanowires on Si substrates grown by solid source molecular beam epitaxy, *Nanotechnology*, 18, 355603.

Jiang, X.; Xiong, Q. Nam, S.; Qian, F.; Li, Y. & Lieber C.M. (2007). InAs/InP radial nanowire heterostructures as high electron mobility devices. *Nano Lett.,* 7, 3214-3218.

Largeau, L.; Dheeraj, D.L.; Tchernycheva, M.; Cirlin, G.E. & Harmand, J.C. (2008). Facet and in-plane crystallographic orientations of GaN nanowires grown on Si(111), *Nanotechnology,* 19, 155704.

Lauhon, L.J.; Gudiksen, M.S.; & Lieber, C.M. (2004). Semiconductor nanowire heterostructures, *Phil. Trans. R. Soc. Lond.* A, 362, 1247–1260.

Martelli, F.; Piccin, M.; Bais, G.; Jabeen, F.; Ambrosini, S.; Rubini, S.; & Franciosi, A. (2007). Photoluminescence of Mn-catalyzed GaAs nanowires grown by molecular beam epitaxy, *Nanotechnology,* 18, 125603.

Meyer, B.K.; Hofmann, D.M.; Volm, D.; Chen, W.M.; Son, N.T.; Janzén, E.; (2001). Optically detected cyclotron resonance investigations on 4*H* and 6*H* SiC: Band-structure and transport properties, *Phys. Rev. B*, *61*, 4844-4849.

Minot, E.D.; Kelkensberg, F.; Van Kouwen, M.; Van Dam, J.A.; Kouwenhoven, L.P.; Zwiller, V.; Borgström, M.T.; Wunnicke, O.; Verheijen, M.A. & Bakkers, E.P.A.M. (2007). Single quantum dot nanowire LEDs. *Nano Lett.,* 7, 367-371.

Moewe, M.; Chuang, L.; Crankshaw, S.; Chase, C. & Chang-Hasnain, C. (2008). Atomically sharp catalyst-free wurtzite GaAs/AlGaAs nanoneedles grown on silicon, *Appl. Phys. Lett*., 93, 23116.

Moses, A.F.; Hoang, T.B.; Dheeraj, D.L.; Zhou, H.L.; van Helvoort, A.T.J.; Fimland, B.O. & Weman, H. (2009). Micro-photoluminescence study of single GaAsSb/GaAs radial and axial heterostructured core-shell nanowires, IOP Conf. Series: Materials Science and Engineering 6, 012001.

Mujica, A.; Needs, R. & Munoz, A. (1995). First-principles pseudopotential study of the phase stability of the III-V semiconductors GaAs and AlAs, *Phys. Rev. B,* 52, 8881.

Murayama, M. & Nakayama, T. (1994). Chemical trend of band offsets at wurtzite/zinc-blende heterocrystalline semiconductor interfaces, *Phys. Rev. B,* 49, 4710-4724.

Pemasiri, K.; Montazeri, M.; Gass, R.; Smith, L.M.; Jackson, H.E.; Yarrison-Rice, J.; Paiman, S.; Gao, Q.; Tan, H.H.; Jagadish, C.; Zhang, X. & Zou, J. (2009). Carrier dynamics and quantum confinement in type II ZB-WZ InP nanowire homostructures, *Nano Lett.,* 9, 648-654.

Patriarche, G.; Glas, F.; Tchernycheva, M.; Sartel, C.; Largeau, L. & Harmand, J.C. (2008). Wurtzite to zinc blende phase transition in GaAs nanowires induced by epitaxial burying, *Nano Lett*, 8,1638-1643.

Phillips, J.C. (1973). Bonds and bands in semiconductors (Academic Press, New York and London, 1973).

Plante, M.C. & LaPierre, R.R. (2006). Growth mechanisms of GaAs nanowires by gas source molecular beam epitaxy, *J. Cryst. Growth,* 286, 394–399.

Schmidt, V.; Wittemann, J.V.; Senz, S.; & Gösele, U. (2009). Silicon nanowires: A review on aspects of their growth and their electrical properties. *Adv. Mater.* 21, 2681-2702.

Shitara, T.; Neave, J.H.; & Joyce, B.A. (1993). Reflection high-energy electron diffraction intensity oscillations and anisotropy on vicinal AlAs(001) during molecular-beam epitaxy, *Appl. Phys. Lett.,* 62, 1658.

Shtrikman, H.; Popovitz-Biro, R.; Kretinin, A. & Heiblum, M. (2009). Stacking-faults-free zinc blende GaAs nanowires, *Nano Lett.,* 9, 215-219.

Soshnikov, I. P.; Cirlin, G. E.; Dubrovskii, V. G.; Veretekha A. V.;, Gladyshev, A.G. & Ustinov, V.M. (2005). Formation of GaAs nanowhisker arrays by magnetron sputtering deposition, *Phys. Solid State*, 48, 786–791.

Svensson, C.P.T.; Mårtensson, T.; Trägårdh, J.; Larsson, C.; Rask, M.; Hessman, D.; Samuelson, L. & Ohlsson, J. (2008) Monolithic GaAs/InGaP nanowire light emitting diodes on silicon. *Nanotechnology,* 19, 305201.

Takeuchi, S. & Suzuki, K. (1999). Stacking fault energies of tetrahedrally coordinated crystals, *Phys. Status Solidi. A,* 171, 99-103.

Tchernycheva, M.; Cirlin, G.E.; Patriarche, G.; Travers, L.; Zwiller, V.; Perinetti, U. & Harmand, J.C. (2007). Growth and characterization of InP nanowires with InAsP insertions, *Nano Lett.*, 7, 1500-1504.

Tian, B.; Kempa, T.J.; & Lieber, C.M. (2009). Sinlge nanowire photovoltaics. *Chem. Soc. Rev.*, 38, 16–24.

Titova, L.; Hoang, T.; Jackson, H.; Smith, L.; Yarrison-Rice, J.; Kim, Y.; Joyce, H.; Tan, H. & Jagadish, C. (2006). Temperature dependence of photoluminescence from single core-shell GaAs–AlGaAs nanowires, *Appl. Phys. Lett.,* 89, 173126.

Tomioka, K.; Kobayashi, Y.; Motohisa, J.; Hara, S. & Fukui, T. (2009). Selective-area growth of vertically aligned GaAs and GaAs/AlGaAs core–shell nanowires on Si(111) substrate, *Nanotechnology,* 20, 145302.

Van Helvoort, A.T.J.; Dheeraj, D.L.; Grønsberg, S.; Zhou, H.L.; Fimland, B.O. & Weman, H. (2009). Dark field transmission electron microscopy techniques for structural characterization of nanowire heterostructures, accepted for publication in *J. Phys: Conf. Series (EMAG2009)*.

Wagner, R.S. & Ellis, W.C. (1964). Vapor-liquid-solid mechanism of single crystal growth. *Appl. Phys. Lett.*, 4, 89.

Wu, Y. & Yang, P. (2001). Direct observation of vapor-liquid-solid nanowire growth *J. Am. Chem. Soc.*, 123, 3165-3166.

Yang, K. & Schowalter, L.J. (1992). Surface reconstruction phase diagram and growth on GaAs(111)B substrates by molecular beam epitaxy, *Appl. Phys. Lett.* 60, 1851-1853.

Yeh, C.Y.; Lu, S.; Froyen, S. & Zunger, A. (1992). Zinc-blende–wurtzite polytypism in semiconductors, *Phys. Rev. B* 46, 10086-10097.

Zanolli, Z.; Fuchs, F.; Furthmüller, J.; von Barth, U. & Bechstedt, F. (2007). Model GW band structure of InAs and GaAs in the wurtzite phase, *Phys. Rev. B*, 75, 245121.

Zhou, H. L.; Hoang, T.B.; Dheeraj, D.L.; van Helvoort, A.T.J.; Liu, L.; Harmand, J.C.; Fimland, B.O. & Weman, H. (2009). Wurtzite GaAs/AlGaAs core–shell nanowires grown by molecular beam epitaxy, *Nanotechnology,* 20, 415701.

IntechOpen

IntechOpen

Nanowires

Edited by Paola Prete

ISBN 978-953-7619-79-4
Hard cover, 414 pages
Publisher InTech
Published online 01, February, 2010
Published in print edition February, 2010

This volume is intended to orient the reader in the fast developing field of semiconductor nanowires, by providing a series of self-contained monographs focusing on various nanowire-related topics. Each monograph serves as a short review of previous results in the literature and description of methods used in the field, as well as a summary of the authors recent achievements on the subject. Each report provides a brief sketch of the historical background behind, the physical and/or chemical principles underlying a specific nanowire fabrication/characterization technique, or the experimental/theoretical methods used to study a given nanowire property or device. Despite the diverse topics covered, the volume does appear as a unit. The writing is generally clear and precise, and the numerous illustrations provide an easier understanding of the phenomena described. The volume contains 20 Chapters covering altogether many (although not all) semiconductors of technological interest, starting with the IV-IV group compounds (SiC and SiGe), carrying on with the binary and ternary compounds of the III-V (GaAs, AlGaAs, GaSb, InAs, GaP, InP, and GaN) and II-VI (HgTe, HgCdTe) families, the metal oxides (CuO, ZnO, ZnCoO, tungsten oxide, and PbTiO3), and finishing with Bi (a semimetal).

How to reference

In order to correctly reference this scholarly work, feel free to copy and paste the following:

D.L. Dheeraj, H.L. Zhou, A.F. Moses, T.B. Hoang, A.T.J. van Helvoort, B.O. Fimland and H. Weman (2010). Heterostructured III-V Nanowires with Mixed Crystal Phases Grown by Au-Assisted Molecular Beam Epitaxy, Nanowires, Paola Prete (Ed.), ISBN: 978-953-7619-79-4, InTech, Available from: http://www.intechopen.com/books/nanowires/heterostructured-iii-v-nanowires-with-mixed-crystal-phases-grown-by-au-assisted-molecular-beam-epita

INTECH
open science | open minds

InTech Europe
University Campus STeP Ri
Slavka Krautzeka 83/A
51000 Rijeka, Croatia
Phone: +385 (51) 770 447
Fax: +385 (51) 686 166
www.intechopen.com

InTech China
Unit 405, Office Block, Hotel Equatorial Shanghai
No.65, Yan An Road (West), Shanghai, 200040, China
中国上海市延安西路65号上海国际贵都大饭店办公楼405单元
Phone: +86-21-62489820
Fax: +86-21-62489821

© 2010 The Author(s). Licensee IntechOpen. This chapter is distributed under the terms of the Creative Commons Attribution-NonCommercial-ShareAlike-3.0 License, which permits use, distribution and reproduction for non-commercial purposes, provided the original is properly cited and derivative works building on this content are distributed under the same license.

IntechOpen

IntechOpen